

Enhanced Third-Order Optical Nonlinearity in a Dipolar Carbene-Metal-Amide Material with Two-Photon Excited Delayed Fluorescence

Ikechukwu D. Nwosu,^[1] Lujó Matasović,^[2] Tárcius N. Ramos,^[3] Nguyen Le Phuoc,^[4] Giacomo Londi,^[5] Alexander J. Gillett,^[2] Daniel T. W. Toolan,^[6] Charles T. Smith,^[7] George F. S. Whitehead,^[1] Mireille Blanchard-Desce,^[8] Jonathan Daniel,^{[8]*} Mikko Linnolahti,^{[4]*} Yoann Olivier^{[9]*} and Alexander S. Romanov^{[1]*}

^[1] I.D. Nwosu, G.F.S. Whitehead, A.S. Romanov, Department of Chemistry, the University of Manchester, Oxford Rd., Manchester M13 9PL, UK

^[2] L. Matasović, A.J. Gillet, Cavendish Laboratory, Department of Physics, University of Cambridge, J J Thomson Avenue, CB3 0HE, UK

^[3] T.N.Ramos, Theoretical Chemistry Laboratory, Namur Institute of Structured Matter, Université de Namur Rue de Bruxelles, 61, 5000 Namur, Belgium

^[4] N.L. Phuoc, M. Linnolahti, Department of Chemistry and Sustainable Technology, University of Eastern Finland, FI-80101 Joensuu, Finland

^[5] G. Londi, Department of Chemistry and Industrial Chemistry, University of Pisa, 56124, Pisa, Italy

^[6] D.T.W. Toolan, Department of Materials, the University of Manchester, Oxford Rd., Manchester M13 9PL, UK

^[7] C.T. Smith, Department of Physics and Astronomy and the Photon Science Institute, the University of Manchester, Oxford Road, Manchester, M13 9PL, UK

^[8] J. Daniel, M. Blanchard-Desce, Institut des Sciences Moléculaires (ISM, UMR5255), University of Bordeaux, Centre National de la Recherche Scientifique, Institut Polytechnique de Bordeaux, Bat A12, 351 Cours de la Libération, 33405 Talence, France

^[9] Y. Olivier, Laboratory for Computational Modeling of Functional Materials Namur Institute of Structured Matter, Université de Namur Rue de Bruxelles, 61, 5000 Namur, Belgium

* Correspondence to

alexander.romanov@manchester.ac.uk

mikko.linnolahti@uef.fi

yoann.olivier@unamur.be

jonathan.daniel@u-bordeaux.fr

Keywords: Photoluminescence, two-photon absorption, TADF, nonlinear optics, carbene complex, gold

Abstract

Advanced photonic materials showing two-photon absorption (2PA) have been widely explored to develop three-dimensional imaging, micro and nanofabrication, all-optical switching, lithography on a nanoscale and many other enabling technologies. These all require nonlinear absorption chromophores with intrinsic 2PA cross-sections and long-term photo- and thermal stability. Here, we disclose the very first example of the dipolar carbene-metal-amide (CMA) material showing an enhanced 2PA cross-section up to 105 GM. Overall molecular design considerations such as extended π -conjugation (to increase polarizability), minimizing the singlet-triplet energy gap (ΔE_{ST}), and using heavy metal atoms are the first design principles to obtain bright one- and two-photon excited thermally activated delayed fluorescence (TADF) material, showing one of the highest radiative rate of $2.18 \cdot 10^6 \text{ s}^{-1}$ across CMA materials. Bright red CMA 2P-TADF material shows excellent photostability ($LT_{50} = 3 \text{ h}$) to 20 mW femtosecond pulsed laser excitation at 1000 nm, encouraging further CMA exploration for future applications in advanced photonic technologies requiring third-order nonlinear optical properties.

Introduction

Photonic materials with high third-order nonlinear optical (NLO) response such as two-photon absorption (2PA) and two-photon excited fluorescence (2PEF) are highly sought after for a variety of advanced optical technologies in data storage,¹ multi-photon microscopy,² imaging,³ photodynamic therapy,⁴ two-photon nanolithography,⁵ all-optical switching,⁶ and optical power limiting.⁷ Unlike conventional one photon absorption (1PA, Figure 1a) where a single photon possesses enough energy to enable the $S_0 \rightarrow S_1$ electronic transition, 2PA relies on the combined energy of two photons that must hit the molecule simultaneously within few femtoseconds according to the Heisenberg's uncertainty principle under the single intermediate state's approximation (Figure 1a, where the photon energy equals or is slightly above one half of the energy gap).⁵ The probability of the optical transition pumped by 2PA depends on the square of the light intensity and is characterized by the 2PA cross-section (σ_2) measured in Göppert-Mayer units (GM, $1 \text{ GM} = 10^{-50} \text{ cm}^4 \text{ s}$

photon⁻¹). Conventional 2PEF materials are limited only by singlet harvesting mechanism, while two-photon excited thermally activated delayed fluorescence (2P-TADF) materials harvest all singlet and triplet excitons offering a unique advantage and high 2PA brightness ($\sigma_2 \times \text{PLQY}$, photoluminescence quantum yield) required for practical applications. This newly emerged interest in such multifunctional materials aims to develop advanced 2P-TADF materials with superior performance.⁸

Molecular design strategies towards brighter 2PA chromophores rely on various combinations of the Donor (D), Acceptor (A) moieties and π -conjugated bridge to form a dipolar (D- π -A, V-shaped D- π -A- π -D or A- π -D- π -A), quadrupolar (linear D- π -A- π -D or A- π -D- π -A), octupolar or multipolar materials which facilitates the charge transfer (CT) process.⁹ Multiple studies have revealed that quadrupolar and octupolar molecules exhibit much brighter 2PA compared with their dipolar analogues.¹⁰ Such 2PA σ_2 -enhancement has been attributed to much larger polarizabilities for the intramolecular CT state and coherent coupling between branches of the chromophore under the Frenkel exciton model.⁹ Based on this design approach, Xu and co-workers¹¹ synthesized a sky-blue emitting bis(styryl)benzene quadrupolar chromophore (Figure 1b) with heavy bromine atoms to enhance spin-orbit coupling for efficient triplet harvesting. This molecule exhibited a high 2PA cross-section value of 450 GM at 800 nm, attributed to large changes in the quadrupole moment upon excitation, and sufficient π -conjugation giving rise to CT excited states. Adachi et al.⁸ designed bright multipolar 2P-TADF emitters where molecule TPCz2NP (Figure 1c) with extended π -conjugation demonstrated large 2PA cross-section up to 143 GM at 850 nm and explaining 2P-TADF due to efficient delayed fluorescence from a hybrid CT/locally-excited (LE) state. Organometallic 2PA materials are well-represented by various alkynyl and aryl complexes of gold(I), ruthenium(II), and platinum(II) which demonstrated particularly strong 2PA cross-section on par with organic materials up to 10⁴ GM for octupolar and multipolar chromophores.¹² In particular, 4d- and 5d-transition metal complexes are the most promising 2PA and 2PEF candidates due to their electron-rich nature and greater polarizability compared with 3d-metal complexes.¹⁰ Unfortunately, the majority of the metal complexes are limited by 2PA fluorescence or long-lived phosphorescence with no examples of the 2P-TADF materials to date.¹³

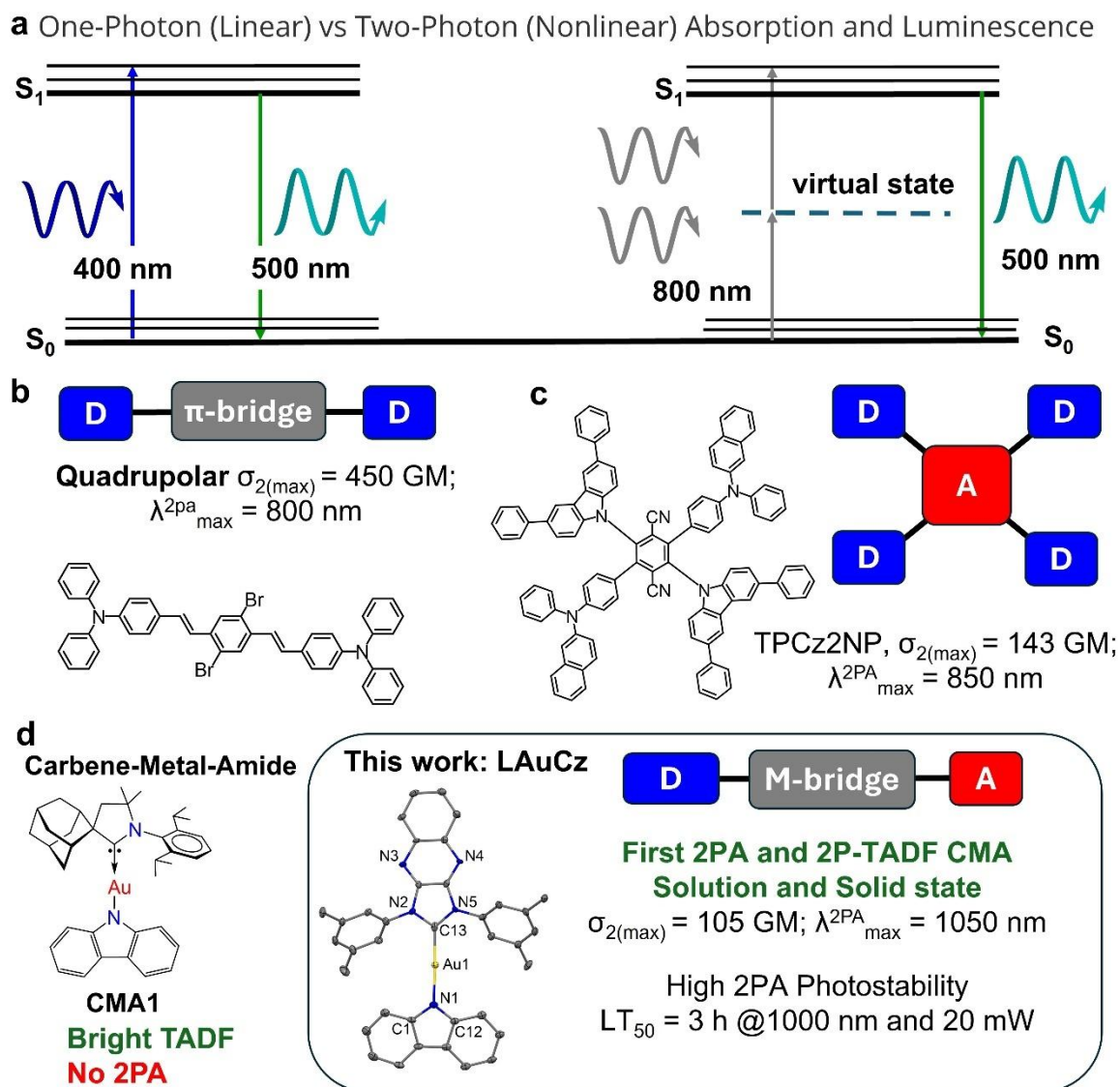


Fig. 1 | The molecular design of different two-photon absorption (2PA) materials including organic TADF molecules with their maximum 2PA cross-sections. (a) Schematic diagram for one- and two-photon absorption and emission processes; (b and c) Molecular structures of the reported 2P-TADF; (d) Molecular structures of Carbene-Metal-Amide (CMA) materials.

A vast majority of 2PA measurements are reported in fluid media, while much less works consider solid-state 2PA measurements due to laser-induced damage of the chromophore or the surrounding polymer matrix.¹⁴ The solid state photostability is a natural limiting factor for a number of advanced photonic technologies such as targeted drug delivery,⁴ two-photon lithography⁵ or all optical switching⁶ to enable fast switching speeds for telecommunication and computing,¹⁵ and enhanced efficiency of photovoltaic cells.¹⁶ Dipolar molecules usually exhibit lower 2PA cross-sections (0.1–50 GM) compared to

quadrupolar molecules (up to 10^4 GM).¹⁷ However, molecular design of the robust dipolar (D- π -A) 2PA chromophores is much more feasible compared to multipolar materials. For instance, Hudson¹⁸ and others¹⁹ demonstrated dipolar organic TADF materials with up to 400 GM 2P TADF in toluene solution which are prone to photodegradation within several hours. Therefore, bright dipolar 2PA chromophores with high thermal- and photostability towards pulsed femtosecond laser excitation are one of the most sought-after 2PA materials. At the best of our knowledge, examples of small dipolar molecules exhibiting both 2PA and TADF in the solid state are not reported in the literature neither for organic nor organometallic systems.

Carbene-metal-amides (CMA, M = Cu, Ag or Au) emerged as bright TADF materials enabling energy-efficient organic light emitting diodes (OLEDs).¹⁹ One of the first successful CMA materials (**CMA1**, Figure 1d) was demonstrated based on a linear Au(I) complex, where the gold atom is coordinated with a cyclic (alkyl)(amino)carbene (CAAC) and a carbazolidine (Cz) ligands. CMA molecular design results in a diminished overlap integrals between the frontier molecular orbitals ($S_{H/L}$) and achieves fast TADF radiative decay rates up to $4 \cdot 10^6$ s⁻¹ with near-unity photoluminescence quantum yields (PLQY).²⁰ Moreover, all CMA molecules shows a substantial difference in the orientation of the ground and excited state dipole moment vectors,¹⁹ indicating large changes in polarization upon photoexcitation, thus showing a great promise to detect 2PA from classical dipolar CMA materials. This fact triggered numerous attempts in our laboratory to discover a champion 2P-TADF CMA material. We demonstrate the very first dipolar CMA material (**LAuCz**, Figure 1d) with enhanced third-order optical nonlinearity, *i.e.* moderate 2PA cross-section and bright 2P-TADF. Proof-of-concept 2PA response for **LAuCz** complex was measured in a solid polystyrene matrix showing enhanced 2PA cross-section up to 105 GM in highly diluted thin films (0.1% by weight). Solid state monoliths of the **LAuCz** complex in polymer shows excellent photostability ($LT_{50} = 3$ h) vs 20 mW femtosecond pulsed laser excitation at 1000 nm. Our findings establish a new CMA molecular design concept by unlocking bright dipolar 2PA-TADF materials and enabling the development of advanced photonic devices and technologies based on third-order nonlinearity response.

Results

Synthesis and structures. Complex **LAuCz** (Figure 1d) was prepared from carbazole and the corresponding chloride complex **LAuCl** in the presence of KO^tBu, following our previously published procedures in high yield.²⁰⁻²³ Compound **LAuCz** is an orange solid soluble in toluene and polar aprotic solvents such as dichloromethane (DCM) and

tetrahydrofuran (THF). The solid samples are stable in air for months and possess high thermal stability up to 307°C (5% weight loss, Supplementary Figure S7). Thermogravimetric analysis (TGA) profile for **LAuCz** samples shows a stepwise decomposition, with the first step accounting for ca. 22% mass loss and attributed to the elimination of the carbazole moiety, based on the 21.6% molecular weight contribution of carbazole. This indicates that the Au–N bond is weaker than the Au–C bond in **LAuCz** complex. The **LAuCz** complex possesses $^{13}\text{C}_{\text{carbene}}$ -carbon resonance at 193.3 ppm, which is downfield-shifted compared to analogous CMA complexes based on pyrazine-fused NHC carbene at 186.8–187.6 ppm.²⁴ This fact suggests less electron shielding for the $\text{C}_{\text{carbene}}$ atom and stronger π -accepting nature of the π -extended quinoxaline-fused NHC ligand. The single crystal X-ray diffraction shows a linear geometry for complex **LAuCz** with the Au–N bond length similar to the benchmark complex **CMA1** whereas Au–C bond is shorter by 0.05 Å for **LAuCz** (Supplementary Table S1). This results in 0.07 Å shorter distance between acceptor(carbene) and donor(amide) ligands for complex **LAuCz** compared to **CMA1**.

Cyclic voltammetry (CV) was carried out in THF (Supplementary Table S1, Figure S9). **LAuCz** shows a quasi-reversible reduction with $E_{1/2}$ at –1.76 V. The energy of the lowest unoccupied molecular orbital (LUMO) is estimated from the reduction profile onset as –3.72 eV. The reduction process is largely localized over the L-carbene ligand which is supported by theoretical calculations (Supplementary Table S1). The LUMO energy of complex **LAuCz** is stabilised by ca. 1 eV compared to benchmark **CMA1** complex (–2.68 eV)²⁰ reflecting the effect of the π -extended backbone of the carbene with two aza-N atoms acting as a strong-electron withdrawing units. **LAuCz** exhibits an irreversible oxidation process at +0.36 V which is higher by 0.09 V compared to benchmark **CMA1** (Supplementary Table S1). This leads to minor difference for the highest occupied molecular orbital (HOMO) energy (–5.62 eV for **LAuCz** and –5.53 eV for **CMA1**, respectively). Complex **LAuCz** exhibits no change in anodic and cathodic current values during multiple reduction scans (30 scans, Supplementary Figure S9), indicating excellent electrochemical stability. The HOMO–LUMO energy gap for **LAuCz** complex of 1.9 eV is nearly 1 eV smaller compared to benchmark **CMA1** (2.85 eV) indicating a strongly red-shifted luminescence for the title complex **LAuCz**.

One-Photon Photophysical Properties.

Complex LMCl. We first collected the UV-visible absorption spectrum for the chloride precursor complex **LMCl** (M = Cu and Au) in various solvents with increasing polarity and performed photophysical characterization (Figure 2, Table 1, Supplementary Figure S10).

The **LCuCl** complex shows a sharp absorption band at 350 nm with extinction coefficients (ϵ) up to $4.0 \times 10^4 \text{ M}^{-1} \text{ cm}^{-1}$ and a broad low-energy absorption band at *ca.* 465 nm with ϵ up to $2.5 \times 10^4 \text{ M}^{-1} \text{ cm}^{-1}$ (Supplementary Figure S10). Unlike copper analogue **LCuCl**, the gold **LAuCl** complex exhibits a vibronically-resolved absorption band at 350 nm with extinction coefficients (ϵ) up to $1.5 \times 10^4 \text{ M}^{-1} \text{ cm}^{-1}$ and weak shoulder at *ca.* 380 nm. All bands for both complexes demonstrate negligible (up to 5 nm) blue-shift upon increasing the solvent polarity. The natural transition orbitals (NTOs) of the relevant transitions are collected in Figure 2c and Supplementary Figure S10. The hole NTO is predominantly localized on metal(I) chloride unit (with 34.3% copper and 21.6% for gold atomic orbitals contribution) while the particle NTO is largely spread across the quinoxaline-carbene ligand. Literature reports for similar carbene-metal(I)-halide complexes²⁵ ascribe the low-energy band to a halide-metal-to-ligand charge-transfer (XMLCT) transition, while the high-absorption band to an excitation having $\pi-\pi^*$ LE character because of the higher extinction coefficients for the latter.²⁶

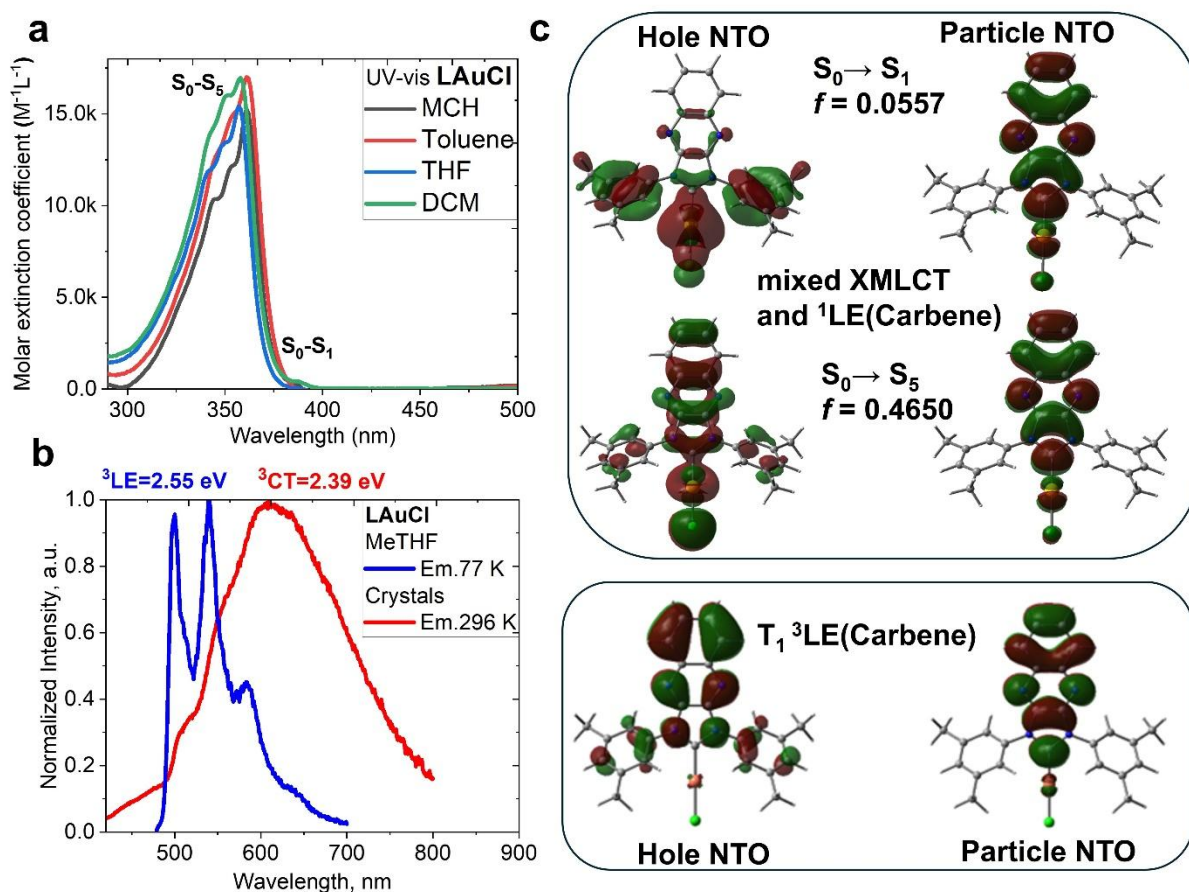


Fig. 2| UV-vis, photoluminescence spectra and natural transition orbitals (NTOs) for gold complex **LAuCl. (a) UV-vis absorption spectra in various solvents; (b)**

Photoluminescence spectra of **LAuCl** in frozen MeTHF at 77 K and crystals at 296 K (excitation at 365 nm); (c) Hole (left) and particle (right) NTO for **LAuCl**.

The photoluminescence profiles for complex **LMCl** are shown in Figure 2b (Table 1, Supplementary Figure S10) for microcrystal powder at room temperature and frozen MeTHF at 77 K. Microcrystals of **LMCl** (M = Cu and Au) emit orange-red light at 639 nm for copper and 607 nm for gold (weak luminescence) with a broad CT-type emission having monoexponential excited-state lifetime of 3 and 111 μ s, respectively. Upon cooling to 77K, the photoluminescence (PL) profile remains broad while the excited-state lifetime increases up to 13 μ s for copper and 18 ms for gold complex. Such minor difference in the PL profile and only several-fold increase in the excited-state lifetime allows us to attribute it to phosphorescence from a 3 XMLCT state with a weakly involved metal center. All solutions of the **LMCl** are non-emissive. However, freezing MeTHF solution of **LMCl** enabled us to detect bright yellow phosphorescence at ca. 500 nm with vibronically resolved profile and very long excited-state lifetime of 32 ms for copper and 5 ms for gold complexes (Figure 2b, Table 1) which is ascribed to a phosphorescence from the triplet 3 LE(carbene) state with an energy of 2.54 eV (Table 1). We corroborated this assignment with TD-DFT calculations (Figure 2c), showing that the NTOs of the triplet excited state are exclusively localized on the carbene ligand (Supplementary Tables S5 and S6).

CMA complex LAuCz. UV-vis absorption spectra for **LAuCz** were measured in solvents with varying polarity: methylcyclohexane (MCH), toluene, tetrahydrofuran (THF) and dichloromethane, as displayed in Figure 3. Complex **LAuCz** shows a sharp, intense band at 350 nm which closely resembles that observed in the precursor material **LCuCl**, showing negligible solvatochromism with ϵ up to $2.5 \times 10^4 \text{ M}^{-1} \text{ cm}^{-1}$, thus attributed to a LE transition mostly involving the carbene unit. The lowest energy band between 400 to 600 nm is broad, unstructured with ϵ up to $12.5 \times 10^3 \text{ M}^{-1} \text{ cm}^{-1}$. This low energy band exhibits up to 65 nm blue-shift upon increasing the solvent polarity from methylcyclohexane to dichloromethane (Figure 3). Such a strong solvatochromism is characteristic for CMA materials^{22,23} reflecting the CT nature of this band for complex **LAuCz**. This empirical observation was corroborated by TD-DFT calculations revealing that this transition has a 1 LLCT character and is dominated (98%) by HOMO to LUMO transition (Figure 4, Supplementary Tables S5 and S6) with the HOMO and LUMO mostly localized on the carbazole and the L-carbene units, respectively, with only weak contribution from the gold atomic orbitals (Supplementary Table S3). The 1 LLCT band blue-shift upon increasing solvent polarity is consistent with the large values for

the ground (9.9 D) and excited state (13.0 D) dipole moments, with latter having the opposite direction (Supplementary Table S4). Overall, CMA complex **LAuCz** has strong potential for 2PA due to its large dipole moment changes upon excitation and high ϵ up to $12.5 \times 10^3 \text{ M}^{-1} \text{ cm}^{-1}$, which reflect strong polarizability of the CMA molecule comparable with other two-photon absorbing organic dyes (ϵ from 10^3 to $10^5 \text{ M}^{-1} \text{ cm}^{-1}$).^{27–29}

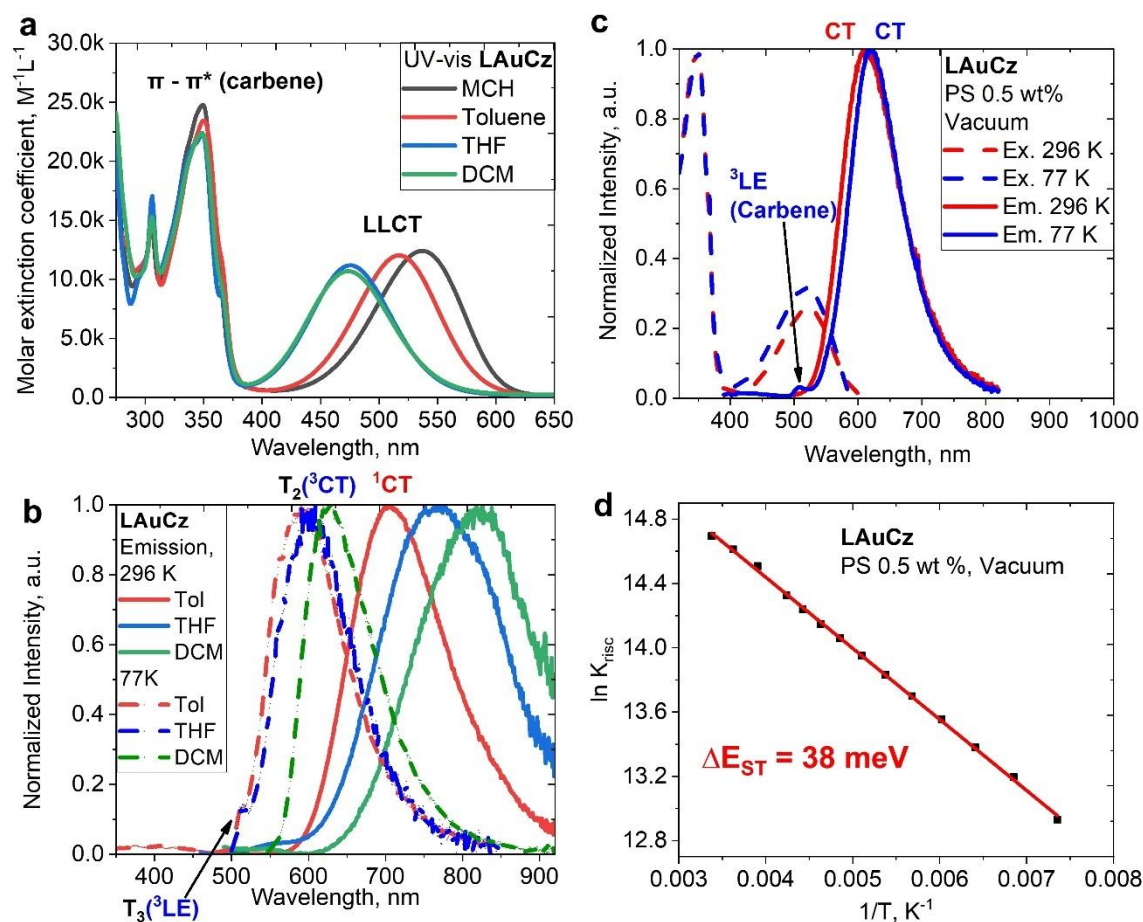


Fig. 3| Photophysical properties of LAuCz complex. (a) UV-visible absorption spectra for **LAuCz** in methylcyclohexane (MCH), toluene, tetrahydrofuran (THF), and dichloromethane (DCM); (b) Emission spectra for **LAuCz** at 296 K (solid lines) and 77 K (dashed lines) in toluene, THF and DCM solution; (c) for 0.5 weight% polystyrene film; (d) Arrhenius fit of temperature dependent decay time profile to estimate a reverse intersystem crossing (rISC) activation energy (ΔE_a).

The photoluminescence of complex **LAuCz** was measured in a 0.5% by weight polystyrene (PS) matrix and solutions with increasing polarity (toluene, THF and dichloromethane, DCM) at 296 and 77 K with data collected in Table 1 (Figure 3b,c). The photoluminescence (PL) of **LAuCz** complex in $1 \cdot 10^{-5} \text{ M}$ toluene solution shows a broad

unresolved emission profile at 706 nm with short excited state lifetime of 112 ns and a moderate PLQY of 19% which is four-times lower compared to the PS film (Table 1). This results in a 12-fold increase for non-radiative processes in fluid media ($k_{nr} = 7.2 \cdot 10^6 \text{ s}^{-1}$) as compared to the solid polystyrene films ($k_{nr} = 0.65 \cdot 10^6 \text{ s}^{-1}$, Table 1). However, flexible environment for **LAuCz** molecules in toluene solution enables greater molecular relaxation and reorganizations in the excited state. This further lowers the energy of the ^1CT state, resulting in 93 nm red-shift into a near-IR region at 767 nm in THF and 826 nm in DCM solutions of complex **LAuCz** due to an increasing solvent polarity which additionally stabilizes a highly polar excited state of CMA molecule. Such a large 120 nm red-shift of the emission for **LAuCz** solutions is paralleled with two-orders of magnitude increase of non-radiative rate from toluene ($k_{nr} = 7.2 \times 10^6 \text{ s}^{-1}$) to DCM ($k_{nr} = 5.2 \times 10^8 \text{ s}^{-1}$), manifesting the energy gap law correlation. In contrast, polystyrene is a rigid host that restricts conformational changes, favouring brighter and higher-energy emission at 613 nm. To demonstrate the impact of the rigid environment on the photoluminescent properties, we measured frozen solutions PL profiles of **LAuCz** (Figure 3b, Table 1), demonstrating up to 200 nm blue-shift and bright luminescence of **LAuCz** as a broad emission profile at 77 K which becomes similar to the PL profile in a PS-matrix, *vide supra*. Upon freezing the solutions of **LAuCz** the emission is dominated by broad phosphorescence from the ^3CT -state as evidenced by *ca.* 400-fold increase of excited state lifetime up to 46 μs (Table 1) indicating that non-radiative processes have been minimized.

At 296 K in PS matrix, complex **LAuCz** shows bright red emission at 613 nm with a high PLQY of 77% and short excited-state lifetime of 354 ns. The PL profile is broad and featureless, indicating a CT emission with one of the highest radiative rates reported across the CMA materials, $k_r = 2.1 \cdot 10^6 \text{ s}^{-1}$ (Table 1). Upon cooling to 77 K, **LAuCz** exhibits a 6 nm blue-shift for the featureless CT profile and low intensity shorter wavelength emission at 507 nm. The latter exhibits an emission lifetime of 719 μs , with energy 2.53 eV determined as an onset of the blue emission profile edge. Note the precursor chloride complex **LAuCl** shows similar energy of 2.54 eV in frozen-MeTHF, *vide supra*. Therefore, we assigned the high energy emission at 507 nm to phosphorescence from the $^3\text{LE}(\text{Carbene})$ state. The CT emission at 619 nm for complex **LAuCz** at 77 K experiences 70-fold excited-state lifetime increase up to 25 μs from 354 ns at room temperature. Such a strong elongation of the excited-state lifetime is characteristic for the TADF CMA materials (Figure 5, Supplementary Figure S11).²⁴ Therefore, we assign the broad, low-energy emission to TADF from a singlet ^1CT state at 2.32 eV. Oxygen quenching experiments has been carried out for **LAuCz**

samples to further confirm the involvement of the triplet states (Supplementary Figure S25) by demonstrating the total quenching of the phosphorescence from $^3\text{LE}(\text{Carbene})$ and reduced intensity of TADF from CT-states.

The luminescent properties for **LAuCz** in PS matrix were measured as a function of temperature to determine the activation energy barrier of the reverse intersystem crossing (rISC) process for TADF. The excited state lifetime of **LAuCz** markedly increases after *ca.* 100 K (Supplementary Figure S11), albeit emission remains as a mix of TADF and phosphorescence. The emission becomes predominantly phosphorescent on cooling down to 16 K as reflected by a dramatic increase in the excited state lifetime up to 147 μs . A plateau corresponding to pure phosphorescence has not been reached at 16 K, suggesting that TADF remains present even at such a low temperature. We directly fit the temperature-dependent PL decay curves to the Arrhenius equation of $\ln k_{\text{rISC}}$ vs $1/T$ (Figure 3d) based on a two-level S_1/T_1 model³⁰ to estimate the singlet-triplet gap (ΔE_{ST}) of **LAuCz** as 38 meV. The benchmark **CMA1** material exhibits a two-times larger ΔE_{ST} value of 69 meV,²⁰ therefore suggesting that **LAuCz** has faster rISC rates. We explain such excellent performance for complex **LAuCz** based on our computational results indicating a smaller overlap integral for **LAuCz** ($S_{\text{H/L}} = 0.26$) compared to benchmark **CMA1** complex ($S_{\text{H/L}} = 0.36$). Small ΔE_{ST} and $S_{\text{H/L}}$ are important but not sufficient criteria to unlock CMA TADF materials with fast radiative rates exceeding 10^6 s^{-1} . We demonstrated based on various **Aza-CMA** materials that the negative energy gap between CT and ^3LE states, $\Delta E(\text{CT}-^3\text{LE})$ is a second key parameter to check. The larger the $\Delta E(\text{CT}-^3\text{LE})$ the faster radiative rates for the CMA emitters. Complex **LAuCz** has $\Delta E(\text{CT}-^3\text{LE})$ equal to -0.2 eV similar to benchmark **CMA1** material explaining high radiative rate of $2.18 \cdot 10^6 \text{ s}^{-1}$. Notably, the radiative rate surpasses the non-radiative rate, $k_{\text{nr}} = 0.65 \cdot 10^6 \text{ s}^{-1}$, suggesting a high rigidity of the geometry of **LAuCz** molecule in the PS matrix once in the excited state.

Transient PL decay analysis enabled estimation of the prompt fluorescence (PF) excited state lifetime of *ca.* 600 ps which is four-orders of magnitude faster compared to delayed fluorescence (DF) of 354 ns (Figure S24). The key TADF rate constants (Table S11) were calculated using a well-established model.³¹ The k_{rISC} value was estimated as $1.67 \times 10^9 \text{ s}^{-1}$, which is close similar with other CMA emitters ($0.8\text{--}3.5 \times 10^9 \text{ s}^{-1}$)³² and orders of magnitude faster compared to classical organic TADF and 2P TADF molecules ($k_{\text{rISC}} = 10^4\text{--}10^6 \text{ s}^{-1}$). High k_{rISC} of **LAuCz** is attributed to near thermal equilibrium between singlet and triplet LLCT excited states and strong spin-orbit coupling of the bridging gold(I) atom. Such a fast k_{rISC} rate translates into superior photostability of the **LAuCz** (0.1 wt.% doped PS film,

Figure 5e) compared to benchmark organic TADF emitter **4CzIPN**. Under constant exposure to 375 nm UV light, the PS films of the title complex show almost no photodegradation under vacuum with only small photodegradation in air (LT_{93} of 6 h, where LT_{93} is time taken to reduce initial brightness by 7%). These results demonstrate that higher k_{rISC} rate of the organometallic TADF compared to organic TADF emitters effectively reduces photodegradation rate and enhances TADF properties in thin film.¹⁹ This superior photostability is also beneficial for improving the 2P TADF photostability, *vide infra*, which is crucial for future practical applications.

Table 1 | Photoluminescent properties of **LMCl** (M = Cu and Au) and **LAuCz** in as a microcrystalline solid, 0.5% by weight polystyrene matrix (PS), and toluene, THF, DCM solution at 296 and 77 K.

	λ_{em} (nm)	τ (μ s)	Φ (%) ^a	k_r (10^6 s ⁻¹) ^b	k_{nr} (10^6 s ⁻¹) ^c	³ CT/ ¹ CT/ ³ LE (eV) ^{d,e}	λ_{em} (nm, 77 K)	τ (μ s, 77 K)
Crystals, 296 K							Frozen MeTHF Glass	
LCuCl	639	3	15	0.05	0.28	2.22/-/2.54	550	32000
LAuCl	607	111	<1	–	–	2.39/-/2.54	500	5127
0.5 wt.% PS matrix, 296 K							0.5 wt. % PS matrix, 77 K	
LAuCz	613	0.354	77	2.18	0.65	2.25/2.32/2.53	619	25
							507	719
LAuCz solution, 296 K							Toluene, 77 K	
Toluene	706	0.112	19	1.70	7.23	2.40/2.07/2.49	593	46
								2900
THF	767	0.0066	3.7	5.61	145.9	2.36/2.00/2.49	602	35.3
DCM	826	0.0019	0.9	4.74	521	2.20/1.89/-	627	16.9

^a Absolute quantum yields determined using an integrating sphere; ^b Radiative rate constant $k_r = \Phi / \tau$; ^c Nonradiative constant $k_{nr} = (1 - \Phi) / \tau$. In case of two-component lifetime τ an average was used: $\tau_{av} = (B_1 / (B_1 + B_2))\tau_1 + (B_2 / (B_1 + B_2))\tau_2$, where B_1 and B_2 are the relative amplitudes for τ_1 and τ_2 , respectively; ^d For **LCuCl**, energy of ³CT and ³LE states are obtained from onset values of the emission spectra blue edge in crystals at 296 K and MeTHF glasses at 77 K respectively; ^e For **LAuCz**, energy of ¹CT, ³CT and ³LE states are based on the onset values of the emission spectra blue edge in 0.5 weight % polystyrene matrix and toluene at 296 (¹CT), 77 K (³CT).

Excited-state TD-DFT calculations were performed to investigate the energetic ordering and nature (CT or LE) of the excited states of the **LAuCz** complex (Figure 4, Supplementary Tables S5 and S6). The reference material **CMA1** shows first singlet (S_1) and triplet (T_1) excited states with CT character while the second triplet (T_2) excited state is commonly locally excited amide ligand ${}^3\text{LE}(\text{amide})$.^{20,23} Up to now, all complexes followed such ordering. On the contrary, the first two triplet states (T_1 and T_2) of **LAuCz** exhibit a CT character originating from HOMO \rightarrow LUMO and HOMO-1 \rightarrow LUMO transitions, respectively, while T_3 corresponds to the ${}^3\text{LE}$ state located on the π -extended quinoxaline-carbene ligand. The calculated spin-orbit coupling matrix elements (SOCME, cm^{-1} , Supplementary Table S7) for complex **LAuCz** are consistently high between singlet and higher energy triplet (T_2 and T_3) states up to 31.3 cm^{-1} (Figure 4). Even though T_2 and T_3 are much higher in energy as compared to T_1 making the direct population of these states unlikely, the large SOCME between S_1 and $T_{2,3}$ together with a large vibronic coupling between T_1 and $T_{2,3}$ could further enhance rISC rate between T_1 and S_1 in the **LAuCz** material.³³

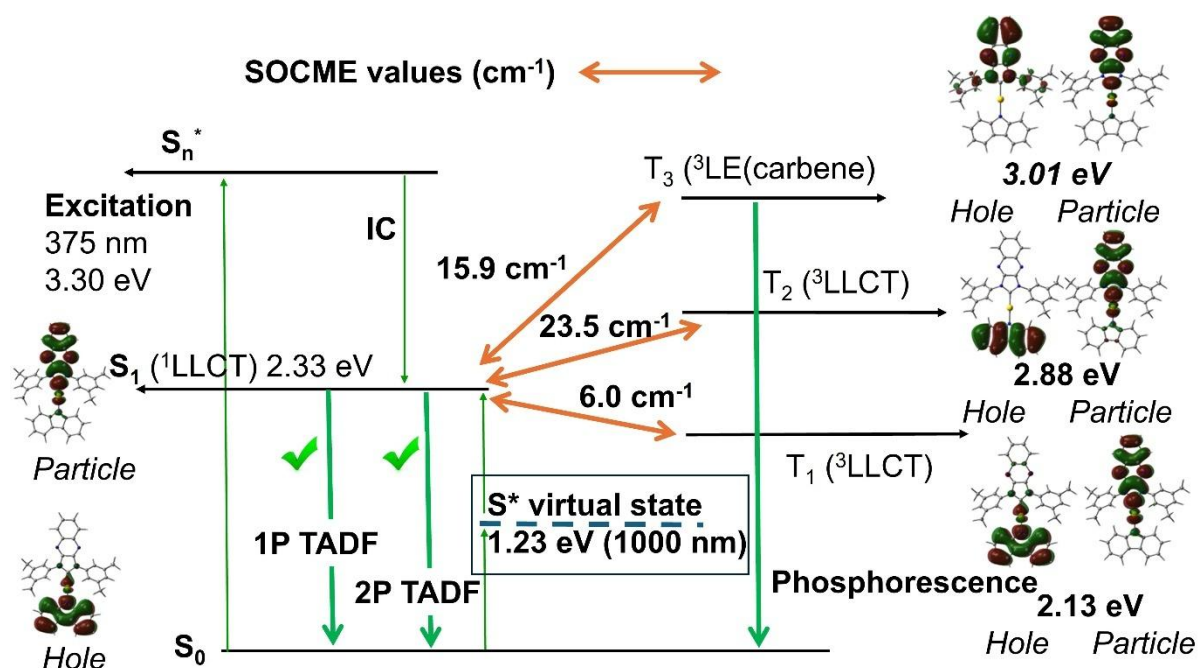


Fig. 4| A Jablonski diagram for complex LAuCz. Excited states energy landscape and NTO (hole and particle) associated to the electronic states S_1 , T_1 , T_2 and T_3 with spin-orbit coupling matrix elements (SOCME, cm^{-1}) for complex **LAuCz**.

Transient Absorption and Two-Photon Absorption. We measure 2PA for **LAuCz** in various media encouraged by its superior radiative rates up to $2.1 \cdot 10^6 \text{ s}^{-1}$, high polarizability and extinction coefficients which are proportional to the square of the transition

dipole moment ($|\mu|^2$) for $S_0 \rightarrow S_1$ transition²⁶ – as one of the conditions for large 2PA cross-sections (σ_2). Thanks to bright TADF from **LAuCz**, the 2PA spectra were measured using 2PEF method in degassed solution (toluene, THF) and polystyrene matrix (PS, 0.1% weight of **LAuCz**), the results are presented on Figure 5. Confirmation of simultaneous two-photon absorption is evidenced by a quadratic dependence between upconverted fluorescence intensity $\text{Log}(F)$ and excitation laser light intensity $\text{Log}(P)$ for compound **LAuCz** (Figures 5b, Supplementary Figures S13–15 for all measured wavelengths from 680 to 1200 nm). The 2PEF of **LAuCz** perfectly overlaps with the 1PA emission (Figure 5c), corroborating TADF nature for the 2PEF signal. Although a low σ_2^{max} value was measured in solution (*ca.* $\sigma_2^{\text{max}} < 0.5$ GM, Figure S11), the 2PA response of **LAuCz** is significantly enhanced in a PS matrix resulting in a moderate 105 GM at 1050 nm -corresponding to an increase of about three orders of magnitudes. Enhanced 2PA cross-section value parallels well with the high radiative rates for complex **LAuCz** in rigid polystyrene matrix that maintains a planar or near-planar geometry. Favourable molecular alignment or aggregation effects lead to significantly enhanced 2PA cross-sections.³⁰ To rule out aggregation enhancement of the TPA TADF for **LAuCz**, grazing incidence wide-angle X-ray scattering (GIWAXS, Supplementary Figure S23) measurements were performed. The scattering pattern of the **LAuCz** in host PS films does not possess any significant ordering that would be commensurate with distinct, **LAuCz** aggregates and that there is no discernible ordering or orientation of the **LAuCz** in the PS host. As a control a neat **LAuCz** film possess significant crystalline features commensurate with distinct crystalline, ordering of **LAuCz**. As such features are not observed in the **LAuCz**:PS blend these GIWAXS measurements enable us to rule out aggregation enhancement in this system.

2PA cross section calculations were carried out at the TD-DFT level of theory in gas-phase and toluene (see the methods section for further details) for **LAuCz** (Supplementary Figure S18–S22 and Supplementary Table S8). The simulated 2PA spectrum in toluene shows a low-energy band centred at ~800 nm (247 GM) composed solely of the S_0 - S_1 excitation, described mainly by a HOMO-LUMO transition. The absence of surrounding polarization in gas-phase decreases the transition energy, the dipole moment, and the transition dipole moment of the **LAuCz**, which are characteristic quantities for charge-transfer excitations and directly connected to the 2PA transition moments. Therefore, the 2PA spectrum in gas-phase results in a red shift of about 100 nm and a decrease of 25 % in the intensity, indicating **LAuCz** 2PA properties are strongly sensitive to the environment.

Besides, the nature of the excitation is not affected by the solvent and remains dominated by a HOMO-LUMO transition. The second and higher-energy band (~450 – 650 nm) comprises several transitions challenging a detailed characterization. Moreover, the incident photon energy approaches the S_0 - S_1 excitation energy, and 1PA resonant effects are expected to contribute to the intensity of the band. The few-states model was applied in order to unravel the dominant and possible interference channels involved in the S_0 - S_1 2PA transition (Supplementary Tables S9 and S10). The two-state model reveals a large S_1 contribution both in toluene (426 GM) and in gas-phase (260 GM) compared to the values obtained using the time-dependent quadratic response formalism. These results are expected due to the observed strong 1-dimensional CT character of the S_0 - S_1 transition, which leads to large transition dipole moments and large variation of the permanent dipole moments in the same direction. Then, considering the five lowest-lying excited states (S_{0-5}), the three-states model shows that the S_5 state is a strong interference channel in toluene, leading to a 2PA cross-section of 333 GM (including S_0 , S_1 , and S_5) and a slight increase of 5 GM for the isolated **LAuCz**. Finally, including the 5 lowest-lying excited states (a six-state model including S_0 - S_5) leads to a value of 330 GM (258 GM), which are larger by a factor of 1.33 (1.39) with respect to the reference value of 247 GM (183 GM) in toluene (isolated) obtained using the time-dependent quadratic response formalism. These results indicate large contributions from high-energetic interference channels beyond the S_5 state and from the surrounding effects. Moreover, these analyses were carried out on a static optimized geometry representing the ground state, and the dynamic effects due to conformational sampling were not addressed.³⁴ Therefore, a lower 2PA cross-section amplitude is expected when considering the dynamic nature of the system in solution³⁵ which would rationalize the difference between the theoretical and the experimental estimates. Furthermore, a direct comparison with the solid-state results is challenging since it would require the adaptation of equations (1 and 3, see Methods) to account for the presence of an anisotropic medium in addition to the simulation of the emitting layer morphology, which are beyond the aim of this study.

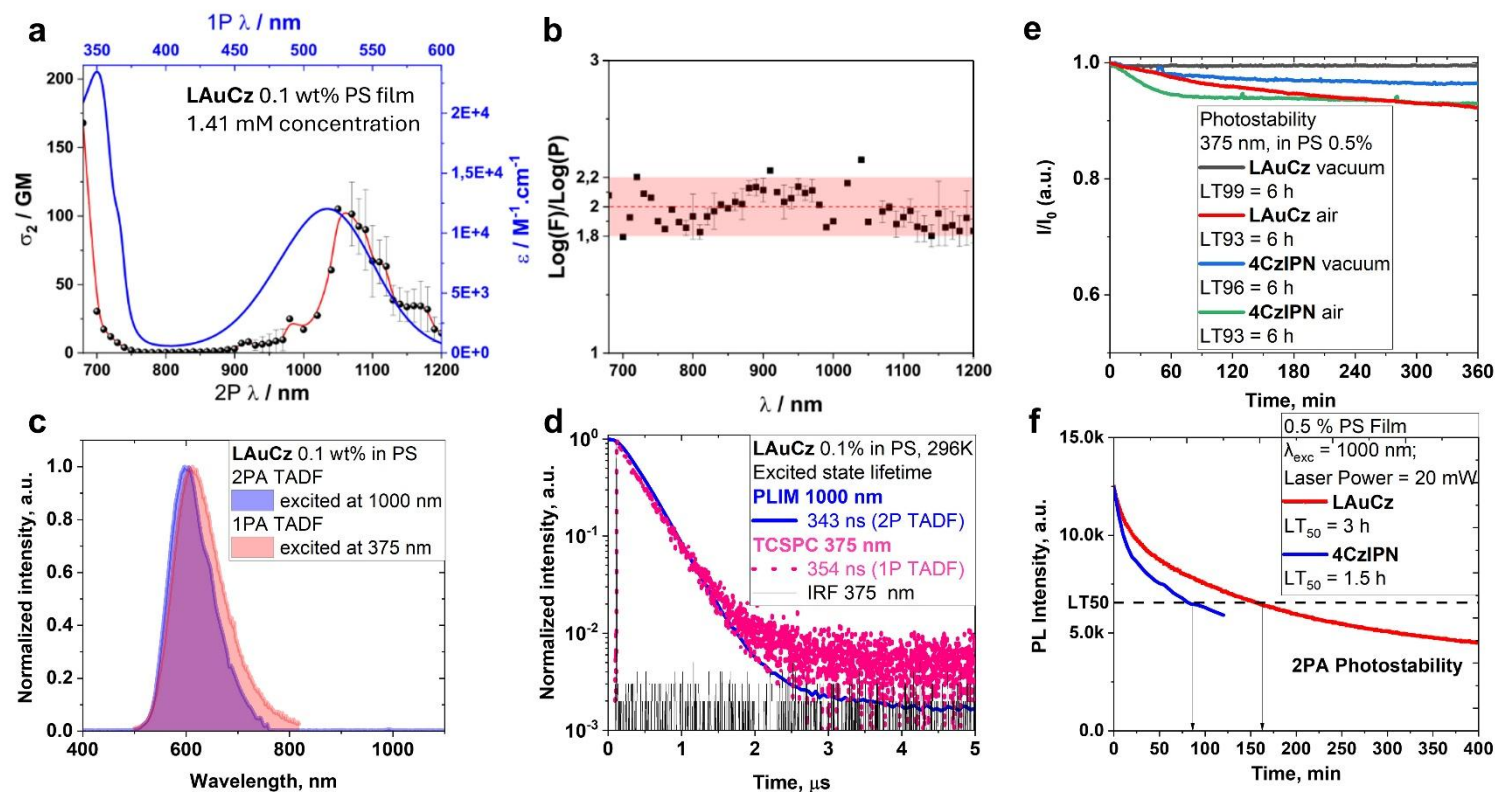


Fig. 5| Photophysical properties of LAuCz complex in 0.1% wt. polystyrene (PS) film under argon. (a) 1PA vs 2PA spectra of LAuCz under argon; **(b)** Quadratic dependence of TADF with excitation power ($\log(F)/\log(P) = 2.0$) for LAuCz. 2PA cross-sections and quadratic dependence are displayed as an average of three ($2P \lambda = 790\text{-}980 \text{ nm}$)³⁶ or four ($2P \lambda = 1070\text{-}1200 \text{ nm}$)³⁷ independent measurements performed on different region in the PS matrix; **(c)** PL profiles for 1PA-TADF and 2P-TADF experiments excited at 375 nm and 1000 nm, respectively; **(d)** Excited state lifetime for 1PA TADF from TCSPC experiment and excited at 375 nm and 2P-TADF excited on PLIM with 1000 nm; **(e)** photostability under constant exposure to the UV-light at 375 nm under vacuum (5×10^{-5} mbar) and air with a comparison to the benchmark 4CzIPN TADF material **(f)** exposure to femtosecond laser 20 mW at 1000 nm under argon atmosphere.

Transient absorption (TA) spectra for complex **LAuCz** in the PS matrix at 298 K are plotted in Figure 6. The spectra on picosecond time scales show the initial excited state absorption at 600–1250 nm within 1 ps. The initial signal observed in TA in the 600 to 800 nm range is predicted from TD-DFT calculations (see methods section for computational details) to arise from the S_1 excited-state absorption. The band centred at 650 nm is associated with triplet states and appears after 100 ps. Calculations revealed that this band could originate from the absorption of either the T_1 or T_2 states while the T_3 state has a very weak absorption and might not be observed in TA-experiment. Moreover, we measured 2PA emission-excitation map indicating that the highest 2PA efficiency can be measured below 680 nm followed by the range from 900 to 1200 nm (Figure 6a) thus in excellent agreement with the singlet and triplet excited state absorptions (Figure 6b).

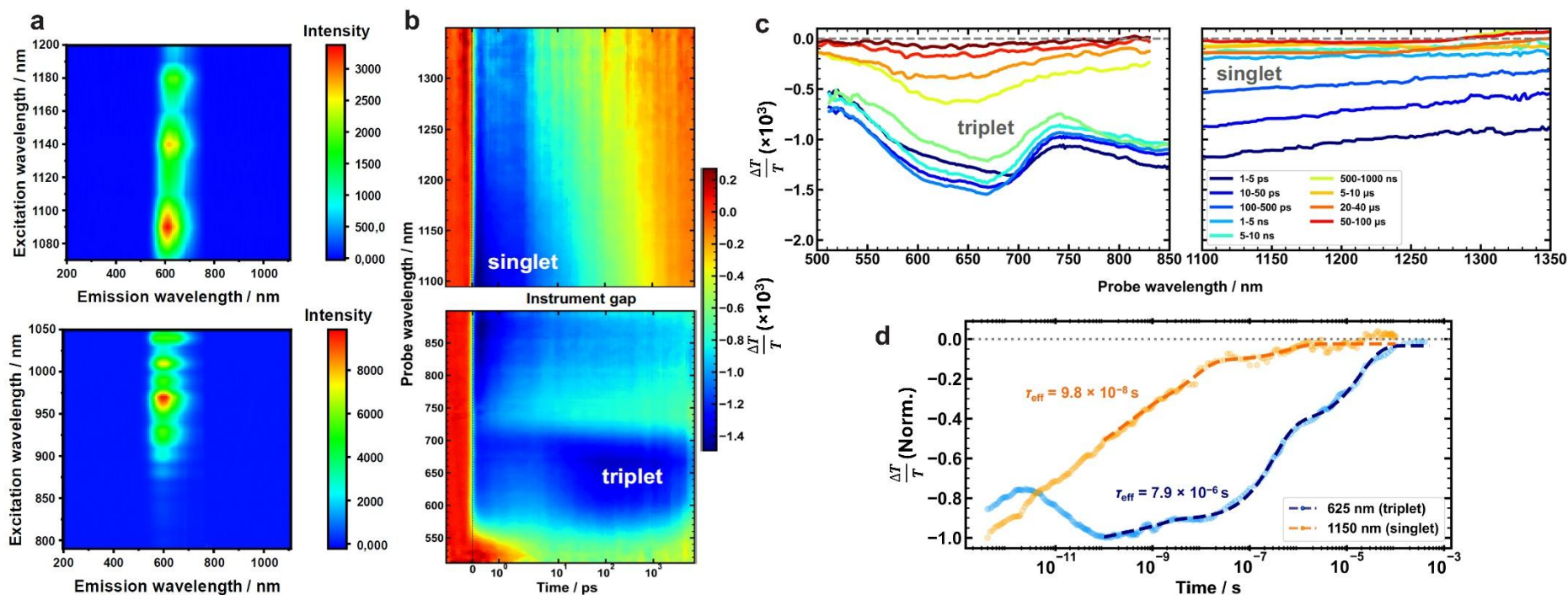


Fig. 6 | 2PA and transient absorption (TA) data for complex LAuCz in a 0.1% wt. polystyrene (PS) film. (a) Log-scaled LAuCz 2PA emission-excitation map; emissions were corrected by input power and emission over 650 nm, where excitation range 680–1050 nm is cropped by short pass optical filter; **(b)** Transient absorption spectroscopy map of LAuCz film (0.1 wt% % load in PS) at room temperature, following 370 nm excitation at a fluence of $9.4 \mu\text{J cm}^{-2}$. PIA bands corresponding to singlet and triplet excitons are centred at 1150 and 625 nm, respectively; **(c)** Time slices of normalised spectra. **(d)** Kinetic traces of singlet and triplet PIAs extracted from picosecond-microsecond TA measurements with corresponding bi- and triexponential fits. After rapid intersystem-crossing, the triplet population peaks around 100 ps.

To reveal the nature of the 2PA emission we first overlaid 1PA profile excited at 375 nm with the 2PA PL profile (850 nm excitation, Figure 5c). Both PL profiles perfectly overlap demonstrating a broad CT emission. Next, we measured 2PA excited state lifetime from complex **LAuCz** in PS film on phosphorescence lifetime imaging setup (PLIM, Figure 5c). Monoexponential fitting and overlay of the traces from the 1PA experiments excited at 375 nm and 1000 nm femtosecond pulsed laser results in nearly identical 1PA (354 ns) and 2PA (343 ns) excited decay time. This decay timescale is attributed to the delayed fluorescence arising from the upconversion of the dark triplet into emissive singlet considering that the prompt fluorescence occurs on a much faster timescale from complex **LAuCz** for both 1PA and 2PA events. Films of **LAuCz** in PS were irradiated by a 1000 nm femtosecond pulsed laser to measure excellent photostability of 3 h (LT_{50}) which opens future 2PA application opportunities in advanced photonic technologies relying on stable materials with strong third-order optical nonlinearity.

Discussion

We present a molecular design strategy for a thermally and photostable dipolar gold CMA complex, representing the first CMA material to exhibit third-order nonlinear optical properties with bright red two-photon-excited TADF (2P-TADF). It was found that benchmark **CMA1** complex, despite possessing a large transition dipole moment ($|\mu|^2$ for $S_0 \rightarrow S_1$) and high TADF radiative rates, fails to emit 2P-TADF, pinpointing that the amphiphilicity of the carbene ligand alone is insufficient. It's the polarizability that must be taken into account; therefore, the use of simultaneously strong ambiphilic and π -extended carbene moieties, for instance, with a quinoxaline backbone, enabled the first proof-of-concept demonstration of highly sought-after solid-state CMA two-photon absorption (2PA) and 2P TADF material.

This success was achieved by doping **LAuCz** complex in the PS matrix, exhibiting an enhanced 2PA cross-section up to 105 GM and photostability ($LT_{50} = 3$ h) towards 20 mW femtosecond pulsed laser excitation at 1000 nm, which is two time longer compared to benchmark **4CzIPN** organic TADF material. It was found that k_{rISC} of **LAuCz** complex ($1.67 \times 10^9 \text{ s}^{-1}$) is orders of magnitude higher compared to classical organic TADF materials thanks to the bridging gold atom with high spin-orbit coupling coefficient. We correlate high k_{rISC} rate for title molecule with a ten-fold higher photostability compared to classical dipolar organic TADF molecules, thanks to faster harvesting of the triplet states. Moreover, 2PA cross-section extends into the near-infrared II region up to 1300 nm with a significant CT

character that enhances the 2PA process, inviting multiphoton absorption experiments in the future. Unlike benchmark material **CMA1**, complex **LAuCz** features a bright carbene-centred ^3LE state which is 0.2 eV above the CT state, while showing a very small ΔE_{ST} of 38 meV and ensuring fast rISC rate for bright red TADF emission in thin films with PLQY up to 77%.

We demonstrated that complex **LAuCz** emits bright red TADF and 2P TADF as a result of the one and two-photon excitation with exceptional radiative rates of up to $2.1 \cdot 10^6 \text{ s}^{-1}$, making **LAuCz** one of the best deep red CMA TADF emitters. The singlet CT nature of the 2PA excitation channel has been confirmed by quantum-chemical calculations and correlated with near-infrared TA measurements and 2PA emission-excitation map. This work establishes molecular design guidelines for developing future bright dipolar 2PA and 2P TADF organometallic chromophores, tailored for advanced photonic applications.

Methods

General.

Computational details

The excited-state S_1 and T_1 structures of the **LAuCz** complex were optimized at the time-dependent density functional theory (TD-DFT) level by using the Tamm-Dancoff approximation (TDA), the exchange-correlation $\omega\text{B97X-D}$ functional, and the 6-31G(d,p) basis set for all the atomic species, except Au for which the def2-TZVP basis set was used along with effective core potential. Excited-state properties were computed at the optimally tuned *screening* range-separated hybrid LC- ωhPBE level of theory in toluene, by using the 6-311G(d,p) basis set for all the atomic species, except for Au (as stated above). For further details we refer to our previous work.³⁸ The Multiwfn³⁹ tool was then used to post-process the Gaussian16⁴⁰ output and to extract excitation energies, oscillator strengths, and transition dipole moments between excited states. Hole-electron density overlaps were estimated by the Φ_s metric, according to the detachment and attachment formalism describe elsewhere.⁴¹ The Supplementary Data 1 contains cartesian coordinates of the optimized structures.

The 2PA cross-section spectra were simulated for the optimized geometry obtained in gas phase. All the 2PA calculations were carried out in Dalton2020.1⁴² software using the CAM-B3LYP DFT functional and the 6-311G(d,p)//def2-TZVP basis sets. The choice of the CAM-B3LYP was based on the requirement of including long-range electronic interactions and was based on direct theoretical-experimental comparisons⁴³⁻⁴⁵ and by benchmarks against high-level Coupled Cluster computations.⁴⁶⁻⁴⁸ 2PA transition probabilities of the first

20 excited states were calculated using the single residue of the time-dependent quadratic response vectors.⁴⁹ In addition, for the few-states models, the permanent dipole moment of the excited states and the transition dipole moments between excited states up to the fifth lowest-lying transitions were computed using the double residue scheme. Solvent effects were taken into account using the continuum FixSol⁵⁰ model implemented in the Polarizable Embedding library.⁵¹ Finally, the 2PA cross-sections were computed assuming a single beam experiment⁴⁶ as given by

$$\sigma_{2PA}^{ng}(\omega) = \frac{4\pi^3 \omega_{ng}^2}{c^2} \delta_{2PA}^{ng} g(2\omega, \omega_{ng}; \Gamma) \quad (1)$$

$$g(2x, \omega_{ng}; \Gamma) = \frac{\sqrt{\ln 2} 2}{\sqrt{\pi} \Gamma} e^{-\frac{\ln 2 (2x - \omega_{ng})^2}{(\Gamma/2)^2}} \quad (2)$$

$$\delta_{2PA}^{ng} = \frac{1}{15} \sum_{i,j=x,y,z} \{S_{ii}^{ng} (S_{jj}^{ng})^* + 2 S_{ij}^{nh} (S_{ij}^{ng})^*\} \quad (3)$$

$$S_{ij}^{ng} = \sum_k \left\{ \frac{\mu_{gk}^i \mu_{kn}^j}{\omega_{ng} - \omega} + \frac{\mu_{gk}^j \mu_{kn}^i}{\omega_{ng} - \omega} \right\} \quad (4)$$

where $\sigma_{2PA}^{ng}(\omega)$ is the spectral contribution from the $g \rightarrow n$ transition with $\hbar\omega_{ng}$ transition energy and δ_{2PA}^{ng} transition probability. c is the speed of light in vacuum, $g(2\omega, \omega_{ng}; \Gamma)$ is a broadening function with a full-width at half-maximum parameter ($\Gamma = 0.3$ eV in this study), S_{ij}^{ng} is the two-photon transition moment, and μ_{ab}^i is the i component of the transition dipole moment between the a, b states or permanent dipole moment when $a = b$.

Data availability

The data that support the plots within this paper and the Supplementary Information and other findings of this study are available from the corresponding authors upon reasonable request.

References.

1. Walker, E. & Rentzepis, P.M., A new dimension. *Nature Photonics*, **2**, 406–408 (2008).
2. Helmchen, F. & Denk, W., Deep tissue two-photon microscopy. *Nature Methods*, **2**, 932–940 (2005).
3. Lesani, P. *et al.* Design principles and biological applications of red-emissive two-photon carbon dots. *Communications Materials* **2**, 108, (2021).

4. Collins, H. A. *et al.* Blood-vessel closure using photosensitizers engineered for two-photon excitation. *Nature Photonics* **2**, 420–424 (2008).
5. Liang, Z. X. *et al.* Two-photon absorption under few-photon irradiation for optical nanoprinting. *Nature Comm.* **16**, 2086 (2025).
6. Giesecking, R.L., Mukhopadhyay, S., Risko, C., Marder, S.R., & Brédas, J.-L., 25th Anniversary Article: Design of Polymethine Dyes for All-Optical Switching Applications: Guidance from Theoretical and Computational Studies. *Adv. Mater.* **26**, 68–84 (2014).
7. Pascal, S., David, S., Andraud, C., & Maury, O. Near-infrared dyes for two-photon absorption in the short-wavelength infrared: strategies towards optical power limiting. *Chem. Soc. Rev.* **50**, 6613–6658 (2021).
8. Mageswari, G.V., Chitose, Y., Tsuchiya, Y., Lin, H.-H., Adachi, C., Rational Molecular Design for Balanced Locally Excited and Charge- Transfer Nature for Two-Photon Absorption Phenomenon and Highly Efficient TADF-Based OLEDs. *Angew. Chem. Int. Ed.* **64**, e202420417 (2025).
9. Katan, et al., Effects of (Multi)branching of Dipolar Chromophores on Photophysical Properties and Two-Photon Absorption. *J. Phys. Chem. A*, **109**, 3024 (2005).
10. Collings, J. C. *et al.* The Synthesis and One- and Two-Photon Optical Properties of Dipolar, Quadrupolar and Octupolar Donor–Acceptor Molecules Containing Dimesitylboryl Groups. *Chem. Eur. J.* **15**, 198–208 (2009).
11. Albota, M. *et al.* Design of Organic Molecules with Large Two-Photon Absorption Cross Sections. *Science* **281**, 1653–1656 (1998).
12. Zhang, L. & Humphrey, M.G. Multiphoton absorption at metal alkynyl complexes. *Coord. Chem. Rev.*, **473**, 214820 (2022).
13. Brannan, A. C. *et al.* Unity Fluorescent Carbene-Gold(I)-Acetylide Complexes with Two-Photon Absorption and Energy-Efficient Blue FOLED. *J. Mater. Chem. C.*, **12**, 13545–13554 (2024).
14. Jensen, L., Mende, M., Schrameyer, S., Jupé, M. & Ristau, D. Role of two-photon absorption in Ta₂O₅ thin films in nanosecond laser-induced damage. *Optics Letters* **37**, 4329–4329 (2012).

15. Price, R.S. *et al.* Polymer Monoliths Containing Two-Photon Absorbing Phenylenevinylene Platinum(II) Acetylide Chromophores for Optical Power Limiting. *ACS Appl. Mater. Interfaces* **7**, 10795–10805 (2015).
16. Cheriton, R. *et al.* Two-photon photocurrent in InGaN/GaN nanowire intermediate band solar cells. *Communications Materials* **1**, 1–7 (2020).
17. Terenziani, F., Katan, C., Badaeva, E., Tretiak, S., Blanchard-Desce, M. Enhanced Two- Photon Absorption of Organic Chromophores: Theoretical and Experimental Assessments. *Adv. Mater.* **20**, 4641–4678 (2008).
18. Elgadi, S.A., Mayder, D.M., Hojo, R., Hudson, Z.M. "Thermally Activated Delayed Fluorescence and Room- Temperature Phosphorescence in Sulfidoazatriangulene-Based Materials and their S-oxides". *Adv. Optical Mater.* **11**, 2202754 (2023).
19. Chitose, Y., Mageswari, G.V., Zenke, R., Ide, T., Kohata, S., Lin, J.-H., Lin, T.-C., Tsuchiya, Y., Adachi, C., "Unlocking Dual Functionality in Triazine-Based Emitters: Synergistic Enhancement of Two-Photon Absorption and TADF-OLED Performance with Electron-Withdrawing Substituents". *Adv. Mater.* 2509857 (2025).
20. Di, D. *et al.* High-performance light-emitting diodes based on carbene-metal-amides. *Science* **356**, 159–163 (2017).
21. Brannan, A.C., Cho, H.-H., Reponen, A.-P. M., Gorgon, S., Phuoc, N.L., Linnolahti, M., Greenham, N.C., Romanov, A.S. Deep-blue and Fast Delayed Fluorescence from Carbene-Metal-Amides for Highly Efficient and Stable Organic Light-Emitting Diodes. *Adv. Mater.* **36**, 2404357 (2024).
22. Li, J. *et al.* Two- Coordinate Copper(I)/NHC Complexes: Dual Emission Properties and Ultralong Room- Temperature Phosphorescence. *Angew. Chem. Int. Ed. Engl.*, **59**, 8210–8217 (2020).
23. Chotard, F., Sivchik, V., Linnolahti, M., Bochmann, M. & Romanov, A.S., Mono- versus Bicyclic Carbene Metal Amide Photoemitters: Which Design Leads to the Best Performance? *Chem. Mater.* **32**, 6114–6122 (2020).
24. Yang, J.-G. *et al.* Highly Efficient Thermally Activated Delayed Fluorescence from Pyrazine- Fused Carbene Au(I) Emitters. *Chem. Eur. J.* **27**, 17834–17842 (2021).

25. Riley, C., Nguyen Le Phuoc, Mikko Linnolahti & Romanov, A. S. Linear Gold(I) Halide Complexes with a Diamidocarbene Ligand: Synthesis, Reactivity, and Phosphorescence. *Organometallics* **43**, 1687–1697 (2023), and references therein.
26. Turro, N. J., Ramamurthy, V. & Scaiano, J. *Modern Molecular Photochemistry of Organic Molecules*. (University Science Books, 2010).
27. Panchompoo, J., Aldous, L., Baker, M., Wallace, M. I. & Compton, R. G. One-step synthesis of fluorescein modified nano-carbon for Pd(II) detection via fluorescence quenching. *The Analyst* **137**, 2054 (2012).
28. Minò, A., Cinelli, G., Lopez, F. & Ambrosone, L. Optical Behavior of Nile Red in Organic and Aqueous Media Environments. *Applied Sciences* **13**, 638–638 (2023).
29. de Reguardati, S., Pahapill, J., Mikhailov, A., Stepanenko, Y. & Rebane, A. High-accuracy reference standards for two-photon absorption in the 680–1050 nm wavelength range. *Optics Express* **24**, 9053 (2016).
30. Valandro, S.R., Jagadesan, P., Feng, F., Schanze, K. Aggregation-Enhanced Two-Photon Absorption of Anionic Conjugated Polyelectrolytes. *J. Phys. Chem. Lett.* **11**, 8292–8296 (2020).
31. Tsuchiya, Y., Diesing, S., Bencheikh, F., Wada, Y., dos Santos, P. L., Kaji, H., Zysman-Colman, E., Samuel, I. D. W., Adachi, C. Exact Solution of Kinetic Analysis for Thermally Activated Delayed Fluorescence Materials. *J. Phys. Chem. A* **125(36)**, 8074–8089 (2021).
32. Tang, R. et al. Au(I)-TADF Emitters for High Efficiency Full-Color Vacuum-Deposited OLEDs and TADF-Sensitized Fluorescent OLEDs with Ultrahigh Brightness and Prolonged Operational Lifetime. *Adv. Optical Mater.* **11**, 2300950 (2023).
33. Valverde, D., et al. Computational Investigations of the Detailed Mechanism of Reverse Intersystem Crossing in Inverted Singlet–Triplet Gap Molecules. *ACS Appl. Mater. Interfaces* **16**, 66991–67001 (2024).
34. Castet, F., Tonnelé, C., Muccioli, L., Champagne, B. Predicting the second-order nonlinear optical responses of organic materials: The role of dynamics. *Acc. Chem. Res.* **55**, 3716–3726 (2022).

35. Ramos, T.N., Franco, L.R., Silva, D.L., Canuto, S. Calculation of the one- and two-photon absorption spectra of water-soluble stilbene derivatives using a multiscale QM/MM approach. *J. Chem. Phys.* **159**, 024309 (2023).
36. Sissa, C., Parthasarathy, V., Drouin-Kucma, D., Werts, M.H.V., Blanchard-Desce, M., Terenziani, F. The effectiveness of essential-state models in the description of optical properties of branched push–pull chromophores. *Phys. Chem. Chem. Phys.*, **12**, 11715–11727 (2010).
37. Makarov, N.S., Drobizhev, M., Rebane, A. Two-photon absorption standards in the 550–1600 nm excitation wavelength range, *Opt. Express* **16**, 4029–4047 (2008).
38. Reponen, A.-P. M., Londi, G., Matthews, C.S.B., Olivier, Y., Romanov, A.S., Greenham, N.C., Gillett, A.J. Understanding Spin-Triplet Excited States in Carbene-Metal-Amides. *Angew. Chem. Int. Ed. Engl.*, **63**, e202402052 (2024).
39. Lu, T., & Chen, F., Multiwfn: A multifunctional wavefunction analyzer. *J. Comput. Chem.*, **33**, 580-592 (2012).
40. Gaussian 16, Revision A.03, M.J. Frisch, et al., Gaussian, Inc., Wallingford CT, 2016.
41. Etienne, T., Assfeld, X., Monari, A., Toward a Quantitative Assessment of Electronic Transitions' Charge-Transfer Character, *J. Chem. Theory Comput.* **10**, 3896–3905 (2014).
42. “Dalton, a molecular electronic structure program, Release Dalton2020.1 (2022), see <http://daltonprogram.org>”.
43. Ramos, T.N., Silva, D.L., Cabral, B.J.C., Canuto, S. On the spectral line width broadening for simulation of the two-photon absorption cross-section of para-nitroaniline in liquid environment, *J. Mol. Liq.* **301**, 112405 (2020).
44. Wielgus, M., Zalesny, R., Murugan, N.A., Kongsted, J., Ågren, H., Samoc, M., Bartkowiak, W. Two-Photon Solvatochromism II: Experimental and Theoretical Study of Solvent Effects on the Two-Photon Absorption Spectrum of Reichardt's Dye, *Chem. Phys. Chem.* **14**, 3731–3739 (2013).
45. Uudsemaa, M., Trummal, A., de Reguardati, S., Callis, P.R., Rebane, A. TD-DFT calculations of one- and two-photon absorption in Coumarin C153 and Prodan: attuning theory to experiment, *Phys. Chem. Chem. Phys.* **19**, 28824–28833 (2017).

46. Beerepoot, M.T.P., Friese, D.H., List, N.H., Kongsted, J., Ruud, K. Benchmarking two-photon absorption cross sections: performance of CC2 and CAM-B3LYP. *Phys. Chem. Chem. Phys.* **17**, 19306–19314 (2015).
47. Paterson, M.J., Christiansen, O., Pawłowski, F., Jørgensen, P., Hättig, C., Helgaker, T., Sałek, P. Benchmarking two-photon absorption with CC3 quadratic response theory, and comparison with density-functional response theory, *J. Chem. Phys.* **124**, 054322 (2006).
48. Naim, C., Zaleśny, R., Jacquemin, D. Two-photon absorption strengths of small molecules: reference cc3 values and benchmarks, *J. Chem. Theory Comput.* **20**, 9093–9106 (2024).
49. Sałek, P., Vahtras, O., Guo, J., Luo, Y., Helgaker, T., Ågren, H. Calculations of two-photon absorption cross sections by means of density-functional theory. *Chem. Phys. Lett.* **374**, 446–452 (2003).
50. Thellamurege, N.M. and Li, H. Note: FixSol solvation model and FIXPVA2 tessellation scheme. *J. Chem. Phys.* **137**, 246101 (2012).
51. Olsen, J.M.H., List, N.H., Steinmann, C., Steindal, A.H., Nørby, M.S., Reinholdt, P. PELib: The Polarizable Embedding library. (2021).

Acknowledgements

A.S.R. acknowledges support from the Royal Society (grant nos. URF\R1\180288, RGF\EA\181008, URF\R\231014), EPSRC (grant code EP/K039547/1 and APP46952). M.L. acknowledges the Academy of Finland Flagship Programme, Photonics Research and Innovation (PREIN), decision 320166, the Finnish Grid and Cloud Infrastructure resources (urn:nbn:fi:research-infras-2016072533). N.L.P. acknowledges the Doctoral Programme in Science, Forestry and Technology (Lumeto, University of Eastern Finland). T.N.R. is a postdoctoral researcher of the Fonds de la Recherche Scientifique – FNRS" (F.R.S.–FNRS). We thank Dr Louise Natrajan, EPSRC and University of Manchester for access the Centre for Radiochemistry Research National Nuclear User's Facility (NNUF, EP/T011289/1) to use FLS-1000 fluorometer. D.T.W.T. acknowledges Diamond Light Source for access to the DL-SAXS equipment (experiment number SM40538-1) supported by an EPSRC grant (EP/R042683/1), and instrument scientist Dr Paul Wady for their help and support during beamtime. L.M. thanks the Winton Programme and Harding Distinguished Postgraduate Scholarship for funding. A.J.G. thanks the Leverhulme Trust for an Early Career Fellowship (ECF-2022-445), the Knut and Alice Wallenberg Foundation for a Wallenberg Academy

Fellows award (KAW 2023.0082), and the Swedish Research Council (VR) for a Starting Grant (2024-03915). European Union's Horizon 2020 research and innovation programme grant agreement no. 101020167 (L.M. and A.J.G.).

Author Contributions

I.D.N. carried out synthesis and characterization, electrochemistry, UV-vis and photoluminescence spectroscopy and analysis, L.M. and A.J.G. performed transient absorption measurements and analysis, D.T.W.T. performed GIWAXS measurements and analysis, T.N.R., N.L.P., G.L., M.L., Y.O. performed theoretical calculations for the ground and excited states and calculations involving a two-photon process, C.T.S. assisted with initial collection of the two-photon absorption data and performed two-photon excited TADF lifetime measurements, G.F.S.W. performed single crystal experiment and refinement, M.B.-D., J.D. and I.D.N. performed two-photon absorption and luminescence experiments in fluid and solid state, A.S.R. conceived and designed the idea. J.D., M.L., Y.O. and A.S.R. planned the project and designed the experiments. I.D.N., Y.O., A.S.R. wrote the manuscript. All authors contributed to the discussion of the results, analysis of the data, reviewed and corrected the manuscript.

Competing Interest

The Authors declare no competing interests.

Fig. 1| The molecular design of different two-photon absorption (2PA) materials including organic TADF molecules with their maximum 2PA cross-sections.

(a) Schematic diagram for one- and two-photon absorption and emission processes; (b and c) Molecular structures of the reported 2P-TADF; (d) Molecular structures of Carbene-Metal-Amide (CMA) materials.

Fig. 2| UV-vis, photoluminescence spectra and natural transition orbitals (NTOs) for gold complex LAuCl.

(a) UV-vis absorption spectra in various solvents; (b) Photoluminescence spectra of LAuCl in frozen MeTHF at 77 K and crystals at 296 K (excitation at 365 nm); (c) Hole (left) and particle (right) NTO for LAuCl.

Fig. 3| Photophysical properties of LAuCz complex.

(a) UV-visible absorption spectra for LAuCz in methylcyclohexane (MCH), toluene, tetrahydrofuran (THF), and dichloromethane (DCM); (b) Emission spectra for LAuCz at 296 K (solid lines) and 77 K (dashed lines) in toluene, THF and DCM solution; (c) for 0.5 weight% polystyrene film; (d) Arrhenius fit of temperature dependent decay time profile to estimate a reverse intersystem crossing (rISC) activation energy (ΔE_a).

Fig. 4| A Jablonski diagram for complex LAuCz.

Excited states energy landscape and NTO (hole and particle) associated to the electronic states S_1 , T_1 , T_2 and T_3 with spin-orbit coupling matrix elements (SOCME, cm^{-1}) for complex LAuCz.

Fig. 5| Photophysical properties of LAuCz complex in 0.1% wt. polystyrene (PS) film under argon.

(a) 1PA vs 2PA spectra of LAuCz under argon; (b) Quadratic dependence of TADF with excitation power ($\log(F)/\log(P)= 2.0$) for LAuCz. 2PA cross-sections and quadratic dependence are displayed as an average of three ($2P \lambda = 790\text{-}980 \text{ nm}$)³⁶ or four ($2P \lambda = 1070\text{-}$

1200 nm)³⁷ independent measurements performed on different region in the PS matrix; (c) PL profiles for 1PA-TADF and 2P-TADF experiments excited at 375 nm and 1000 nm, respectively; (d) Excited state lifetime for 1PA TADF from TCSPC experiment and excited at 375 nm and 2P-TADF excited on PLIM with 1000 nm; (e) photostability under constant exposure to the UV-light at 375 nm under vacuum (5×10^{-5} mbar) and air with a comparison to the benchmark **4CzIPN** TADF material (f) exposure to femtosecond laser 20 mW at 1000 nm under argon atmosphere.

Fig. 6| 2PA and transient absorption (TA) data for complex LAuCz in a 0.1% wt. polystyrene (PS) film.

(a) Log-scaled **LAuCz** 2PA emission-excitation map; emissions were corrected by input power and emission over 650 nm, where excitation range 680–1050 nm is cropped by short pass optical filter; (b) Transient absorption spectroscopy map of **LAuCz** film (0.1 wt% % load in PS) at room temperature, following 370 nm excitation at a fluence of $9.4 \mu\text{J cm}^{-2}$. PIA bands corresponding to singlet and triplet excitons are centred at 1150 and 625 nm, respectively; (c) Time slices of normalised spectra. (d) Kinetic traces of singlet and triplet PIAs extracted from picosecond-microsecond TA measurements with corresponding bi- and triexponential fits. After rapid intersystem-crossing, the triplet population peaks around 100 ps.